Thin-film $(Sb,Bi)_2Se_3$ Semiconducting Layers with Tunable Band Gaps Below 1 eV for Photovoltaic Applications

Thomas Paul Weiss,[1,*] Panagiota Arnou,[1] Michele Melchiorre,[1] Mael Guennou,[1] Daniel Siopa,[1] Christian Pauly,[2] Inmaculada Peral Alonso,[1] Philip J. Dale,[1] and Susanne Siebentritt[1]

[1] *Department of Physics and Materials Science, University of Luxembourg, L-4422 Belvaux, Luxembourg*
[2] *IEE S.A., L-7795 Bissen, Luxembourg*

(Received 13 February 2020; revised 15 June 2020; accepted 2 July 2020; published 6 August 2020)

Polycrystalline $(Sb,Bi)_2Se_3$ thin-film semiconductors are grown by coevaporation with a subsequent annealing process. It is shown that Bi can be incorporated into the Sb_2Se_3 lattice, substituting up to approximately 60% of the Sb atoms, while maintaining the orthorhombic crystal structure. Upon Bi substitution, the lattice expands mainly along the one-dimensional $(Sb,Bi)_4Se_6$ ribbons. In addition, the band gap decreases with a direct (indirect) band gap of 0.891 eV (0.864 eV) for a $(Sb_{0.4},Bi_{0.6})_2Se_3$ thin film. A photovoltaic device based on a $(Sb,Bi)_2Se_3$ absorber is fabricated that displays an open-circuit voltage of 133 mV and a short-circuit current density of 18.4 mA/cm^2, demonstrating the potential of this material for infrared detection or multijunction solar-cell applications.

DOI: 10.1103/PhysRevApplied.14.024014

I. INTRODUCTION

High-quality polycrystalline thin-film semiconducting layers with band gaps between 1.0 and 1.5 eV are available for single-junction photovoltaic applications [1]. Multijunction solar cells with performances beyond the Shockley-Queisser limit [2] require lower band gaps, where, for instance, the ideal band gap of the bottom cell in a tandem structure is approximately 0.9 eV [3].

Furthermore, thin films with band gaps below 1.0 eV are of high interest for infrared sensing applications, in the food sector [4,5], for atmospheric gas detection [6], or in the automotive industry [7], to name a few.

Over the past few decades, the small-band-gap materials (In, Ga)As and (Hg, Cd)Te show the most mature and superior performance for those applications in the short-wave or mid- and long-wave infrared range [8–10]. However, due to the necessity for epitaxy and high temperatures, these approaches are partly incompatible with standard silicon read-out circuits, and therefore, mostly inappropriate for low-cost production.

Instead, optoelectronic technologies based on colloidal quantum dots with tunable band gaps have been extensively studied in recent years, benefiting from simplified device fabrication and potentially low-cost production [11,12]. Recently, short-wave infrared photodiodes based on PbS colloidal quantum dots have shown high detection sensitivities of approximately $D^* = 10^{12}$ Jones at room temperature, which is comparable to the performance of commercial (In, Ga)As detectors [13,14]. However, challenges remain, such as nanocrystal synthesis and stability, the understanding of optoelectronic properties, and the engineering of charge-carrier traps [11] and low carrier mobilities [15].

$(Sb_{1-x}Bi_x)_2Se_3$ polycrystalline thin-film layers are interesting candidates for the photon energy ranges of the applications mentioned above. Without Bi alloying ($x = 0$), Sb_2Se_3 is reported to have a band gap around 1.18 eV [16] and receives increasing interest as a solar-cell material [17], with a promising power conversion efficiency of 9.2% [18]. Li *et al.* report the decrease of the band gap upon Bi incorporation with a value as low as 0.90 eV [19], while keeping the orthorhombic crystal structure of Sb_2Se_3 (ICDD No. 01-083-7429). Wang *et al.* report that $(Sb_{1-x}Bi_x)_2Se_3$ remains in that crystal structure for $x < 0.55$ [20]. For high amounts of Bi ($x > 0.78$), this material is reported to crystallize in the rhombohedral crystal structure $R\bar{3}mR - 3m$ (ICDD No. 00-033-0214) [20] and receives considerable interest as a topological insulator [21,22]. For values of $0.55 < x < 0.78$, the coexistence of both phases is observed [20]. The electron mobility of $(Sb,Bi)_2Se_3$ is reported to be around 15 $cm^2\ V^{-1}\ s^{-1}$ [20], which allows fast electron transport (drift or diffusion), and hence, a fast response time of an infrared detector. Depending on the orientation of the grains, the mobility might even be higher [23].

No photovoltaic device based on a $(Sb_{1-x}Bi_x)_2Se_3$ absorber layer has been reported until now. Here, we

*thomas.weiss@uni.lu

investigate $(Sb_{1-x}Bi_x)_2Se_3$ in the orthorhombic crystal structure. We present the change of the lattice parameters as a function of the Bi composition and demonstrate that the composition range of the orthorhombic phase for thin films extends up to $x = 0.6$. At this composition, the direct band gap decreases to 0.891 eV. In addition, a photovoltaic device is presented, which yields an open-circuit voltage of 133 mV and a short-circuit current density of 18.4 mA/cm^2 under simulated AM1.5G illumination.

II. EXPERIMENT

Polycrystalline thin films of $(Sb_{1-x}Bi_x)_2Se_3$ are prepared in a sequential evaporation and annealing process on Mo-coated soda lime glass (SLG) substrates and on bare SLG substrates. First, a precursor layer is deposited by coevaporation from elemental sources of Sb, Bi, and Se in vacuum. The composition indicated by the variable x is varied by changing the source temperatures of Sb and Bi, where $x = 0$ defines pure Sb_2Se_3, crystallizing in the orthorhombic *Pnma* structure (ICDD No. 01-083-7429) and $x = 1$ pure Bi_2Se_3, crystallizing in the rhombohedral $R\bar{3}m$ phase (ICDD No. 00-033-0214). During growth, Se is supplied in excess and the substrate temperature is kept at 240 °C, as measured with a thermocouple in contact with the backside of one of the SLG/Mo substrates. At this temperature, excess Se is desorbed from the surface, resulting in stoichiometric films concerning the selenium-to-metal ratio. These films are subsequently denoted "as grown." The annealing is carried out *ex situ* in a graphite box placed inside a tube furnace. The temperature is ramped from 25 to 350 °C at 8.5 °C/min and kept at 350 °C for 1 h. The background pressure is set to 1200 mbar of N_2. Additional Se powder is placed next to the sample, to supply a Se-rich annealing atmosphere, which is shown to be beneficial for Sb_2Se_3-based absorbers [24–26]. These annealing conditions yield polycrystalline films with grain sizes in the micrometer range, as shown in Fig. 1. Samples processed in this way are subsequently denoted "annealed std," where std denotes the standard process. A few samples are annealed in another tube furnace with a different temperature control. These annealing processes are carried out at nominally 360 °C for 15 min with 1 mbar N_2 background pressure. The sample shown in this paper originating from this annealing is denoted "annealed low," where low refers to the background pressure of 1 mbar N_2.

Photovoltaic devices are fabricated with the device stack adapted from $Cu(In,Ga)Se_2$ solar cells, which is SLG/Mo/$(Sb,Bi)_2Se_3$/CdS/ZnO/grid, where ZnO consists of a double layer of nominally intrinsic ZnO and Al-doped ZnO. Individual devices are defined by mechanical scribing. For the device presented here, the back contact and the absorber growth are modified, compared with films for structural characterization, as follows: the SLG/Mo substrate is exposed to Se flux at a substrate temperature of 560 °C for 1 h prior to precursor growth to partially selenize the Mo back contact [27]. The precursor is grown without Se, i.e., consists only of metallic precursors of Sb and Bi. Annealing is carried out at 400 °C for 1 h with a N_2 background pressure of 800 mbar.

Compositional analysis is carried out by energy-dispersive x-ray (EDX) spectroscopy at 20 kV acceleration voltage. Elemental standards are used for calibration, resulting in a relative accuracy of 2 at. %. The composition x is calculated by $x = [Bi]/([Sb] + [Bi])$, where [Sb] and [Bi] represent the concentration in atomic percent. The error of x is calculated by taking into account the deviation of the atomic concentrations by 2 at. %.

Transmittance and reflection spectra are recorded using a spectrophotometer in the spectral range from 2400 to 880 nm. An integrating sphere is used to collect specular and diffuse light. The absorption is calculated using Eq. (1), which takes multiple reflections within a freestanding film into account [28,29]:

$$\alpha' = \frac{1}{d}\ln\left(\frac{2T'}{-R^2 + 2R + T'^2 + \sqrt{R^4 - 4R^3 - 2R^2T'^2 + 6R^2 + 4RT'^2 - 4R + T'^4 + 2T'^2 + 1} - 1}\right) \quad (1)$$

where R denotes the measured reflectance and T' is the scaled transmission (see the description below). The thickness, d, of the film is measured from a cross-section electron microscopy image. Transmission and reflection are measured on spots with diameters comparable to the thickness of the SLG substrate (2 mm). Therefore, a considerable amount of photons are expected to be scattered and, as a result, do not enter the integrating sphere, where the photons are detected. This affects mainly the measurement of the transmission as the photons first pass through the $(Sb,Bi)_2Se_3$ layer, subsequently through the 2 mm SLG substrate, and then through the aperture to the integrating sphere. To account for this effect, the transmission is scaled such that the absorbance $A = 1 - R - T'$ equals zero far below the band gap. Here, T' is scaled such that the mean absorbance equals zero in a wavelength range below the band gap. The technique is exemplified in Fig. S2 within the Supplemental Material [30]. It is noted that this procedure can be applied only if the transmission is flat in that wavelength range. A result of this procedure is that the

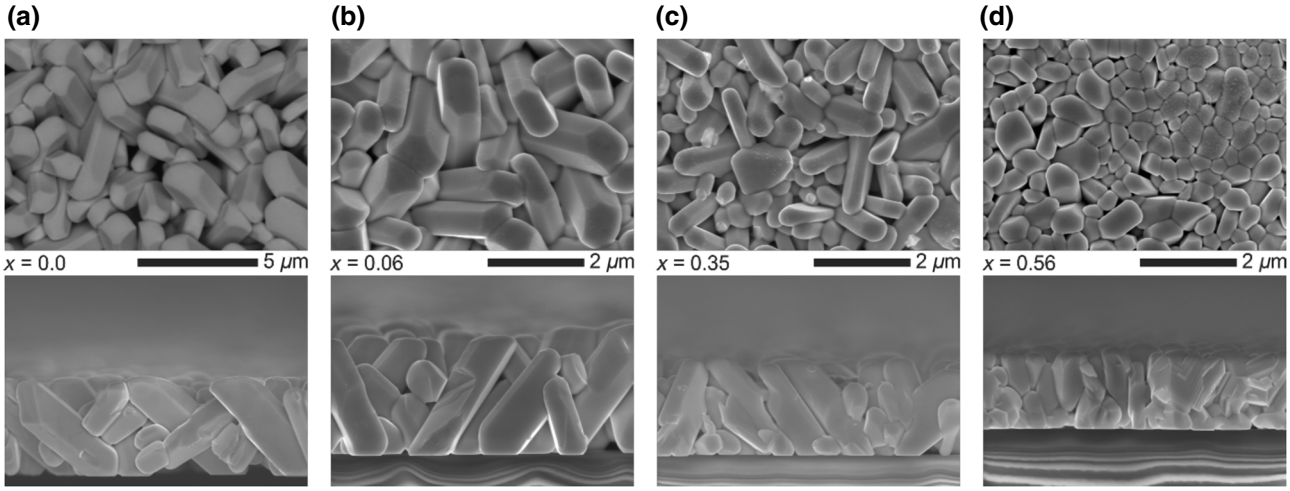

FIG. 1. SEM micrographs of annealed $(Sb_{1-x}Bi_x)_2Se_3$ thin films on a soda lime glass substrate for different compositions in top view (top) and in the cross-section view (bottom). Note the different scale for the sample without any Bi content ($x = 0$). All films crystallize in the orthorhombic structure. Grain size seems to decrease with increasing Bi content.

absorption coefficients approach zero for photon energies well below the band gap. No influence on the determined band gap is observed, regardless of whether T or T' is used (Fig. S2 within the Supplemental Material [30]). From the absorption coefficient, Tauc plots for the direct and indirect band gap are obtained using [31]

$$\alpha' \hbar\omega \propto \sqrt{\hbar\omega - E_{G,\text{direct}}} \tag{2}$$

$$\alpha' \hbar\omega \propto (\hbar\omega - E_{G,\text{indirect}})^2 \tag{3}$$

The direct and indirect band gaps are then obtained by a linear fit of the straight part of the Tauc plot. Errors for the band gaps are obtained by shifting the fitting range by ± 10 meV.

X-ray diffractograms are acquired in Bragg-Brentano configuration with Cu $K\alpha$ radiation in the 2θ range from 10° to 90°. A Ni filter is used to strip the Cu $K\beta$ radiation. The instrumental response function is measured using an Al_2O_3 reference sample. The diffractograms are analyzed using the FullProf_Suite software [32] in the *profile matching with constant scale factor* mode. The diffractograms are fitted using the orthorhombic *Pnma* space group adopted by Sb_2Se_3 (ICDD PDF Card No. 01-083-7429). For a few samples, a two-phase system is observed and, in this case, the secondary phase is fitted with a rhombohedral $R\bar{3}m$ space group, as in pure Bi_2Se_3 (ICDD PDF Card No. 00-033-0214). In the following, these two structures are simply denoted as *orthorhombic* and *rhombohedral*, respectively. Variable parameters for the fitting are the zero shift of the diffractogram, the lattice parameters, and shape parameters. The shape parameters describe the broadening of the diffraction peak by a pseudo-Voigt function, resulting from finite crystallite sizes. Details of this procedure are described in Ref [33].

Photoluminescence (PL) measurements are carried out at room temperature using a 660 nm diode laser as an excitation source focused on the sample surface on a spot with a diameter of approximately 50–100 μm. To ensure a high PL signal, the laser power is set to 100 mW, unless mentioned otherwise. The PL light is collected with two off-axis parabolic mirrors and redirected into a spectrometer via an optical fiber. Inside the spectrometer, the PL light is dispersed and detected by a 512-element (In, Ga)As array. PL signals are spectrally corrected by measuring a reference white-light spectrum in exactly the same setup.

Raman measurements are performed at room temperature with a 532 nm laser excitation wavelength, focused onto the sample with a 50× objective lens and a numerical aperture of 0.5, in combination with a 2400 lines/mm grating. The incident laser has a power density of 760 MW m^{-2} and the spot size is approximately 0.87 μm in diameter. A silicon reference is used for calibration.

Current density-voltage characteristics are recorded under dark conditions and under illumination using a simulated AM1.5G spectrum from a class AAA solar simulator.

External quantum efficiency (EQE) is measured to verify the detection of IR photons. Illumination is provided with chopped monochromatic light, and the current response is measured with a lock-in amplifier. Reference Si and (In, Ga)As photodiodes are used for calibration. Short-circuit conditions and reversed bias voltages are applied for the EQE measurements.

III. MATERIAL PROPERTIES

The lattice parameters of the orthorhombic structure for thin films of $(Sb_{1-x}Bi_x)_2Se_3$ on SLG and SLG/Mo substrates obtained from the XRD refinement are displayed in Fig. 2(a) for compositions between $x = 0$ and 0.76. The

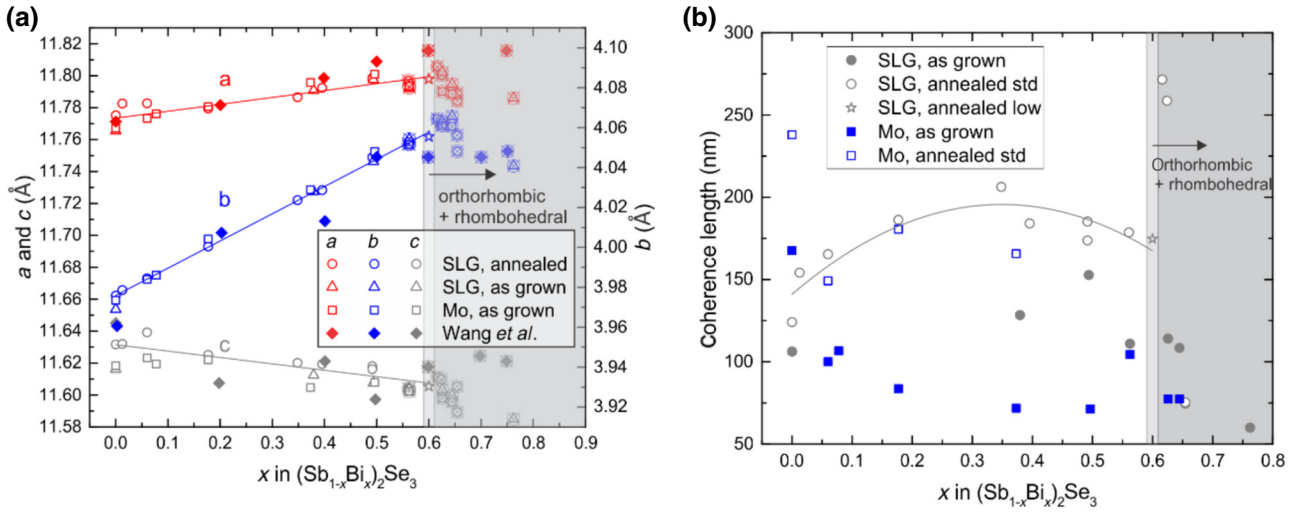

FIG. 2. (a) Lattice parameters a, b, and c of the orthorhombic *Pnma* structure of Sb_2Se_3 with respect to the incorporation of Bi. Data from the literature are added from Wang *et al.* [20]. Open circles with crosses indicate two-phase systems, where the orthorhombic and the rhombohedral phases are observed. Open star at $x = 0.6$ marks the maximum Bi concentration with a pure orthorhombic phase. Light-gray region indicates the confidence in the composition for that data point. (b) Coherence length determined from the XRD peak broadening. Solid gray line is a guide to the eye for the coherence length for layers grown on SLG, annealed std (open gray circles).

lattice parameters for single-phase layers (see discussion below) are linearly fitted (solid lines), resulting in the following expressions, with respect to the compositional parameter x:

$$a(x)/\text{Å} = 11.773(\pm 0.002) + 0.043(\pm 0.006)\, x, \quad (4)$$

$$b(x)/\text{Å} = 3.9759(\pm 0.0007) + 0.136(\pm 0.002)x, \quad (5)$$

$$c(x)/\text{Å} = 11.632(\pm 0.002) - 0.040(\pm 0.007)x. \quad (6)$$

The lattice strain caused by Bi substitution is strongly anisotropic. The linear strain along b, defined as $(db/dx)/b(0) = 34.10^{-3}$, is about 10 times as high as that along a and c ($3.7.10^{-3}$ and $3.4.10^{-3}$, respectively). This indicates that elongation essentially occurs along the direction of the one-dimensional (1D) $(Sb,Bi)_4Se_6$ ribbons (see Fig. S3 within the Supplemental Material [30] for the lattice structure created using VESTA [34]). Samples with a high Bi content ($x \gtrsim 0.6$, marked by the dark gray area in Fig. 2) show additionally the rhombohedral phase. The sample with the highest Bi content and without the rhombohedral phase (single phase) has a composition of $x = 0.60 \pm 0.01$ (light gray area in Fig. 2 highlights the compositional error). This particular sample is grown by both annealing processes, i.e., annealed std and annealed low. The x-ray diffractograms of these two samples and of the as-grown sample are presented in Fig. 3. The orthorhombic structure is clearly present in all three samples. The as-grown sample shows a clear diffraction peak at 18.536°, which can be assigned to the (0 0 6) reflection of the rhombohedral structure. This diffraction peak reduces considerably for the annealed std sample and is below the noise level for the annealed low sample [see Fig. 3(d)]. This shows that the rhombohedral phase can be removed upon annealing (at this composition), and hence, annealing yields a single-phase material. Upon the annealing low process, it is additionally observed that the composition changes towards a higher x value of 0.6 (from 0.56 in the as-grown sample), which might be caused by the high vapor pressure of Sb_2Se_3 [35], and hence, Sb loss.

In a previous study, it was found that samples with $x = 0.6$ already exhibited the rhombohedral phase, while a sample with $x = 0.5$ still showed a single orthorhombic phase [20]. It is then assumed that the single orthorhombic phase can be fabricated up to $x \approx 0.55$. Here, we demonstrate that a single orthorhombic phase can actually be prepared up to $x = 0.6 \pm 0.01$ for polycrystalline thin films. It is interesting to note that Wang *et al.* find that the lattice constant b does not exceed a value of approximately 4.045 Å [20]. However, in the present study, values as high as 4.065 Å are found, indicating that a higher concentration of Bi can be incorporated for a nonequilibrium and thin-film system, i.e., thin films annealed at a rather low temperature (350 °C).

The coherence length calculated from the Scherrer equation (see Sec. II for details) is plotted in Fig. 2(b). Upon annealing, the coherence length increases, and therefore, the crystal quality for both types of substrates, i.e., SLG and SLG/Mo, improves. In addition, the annealed samples grown on SLG show an increase of the coherence length up to $x \approx 0.35$, while this value is decreased for higher x values [see the solid gray line in Fig. 2(b), which serves as a guide to the eye]. This trend of the coherence length indicates that alloying Sb_2Se_3 with Bi

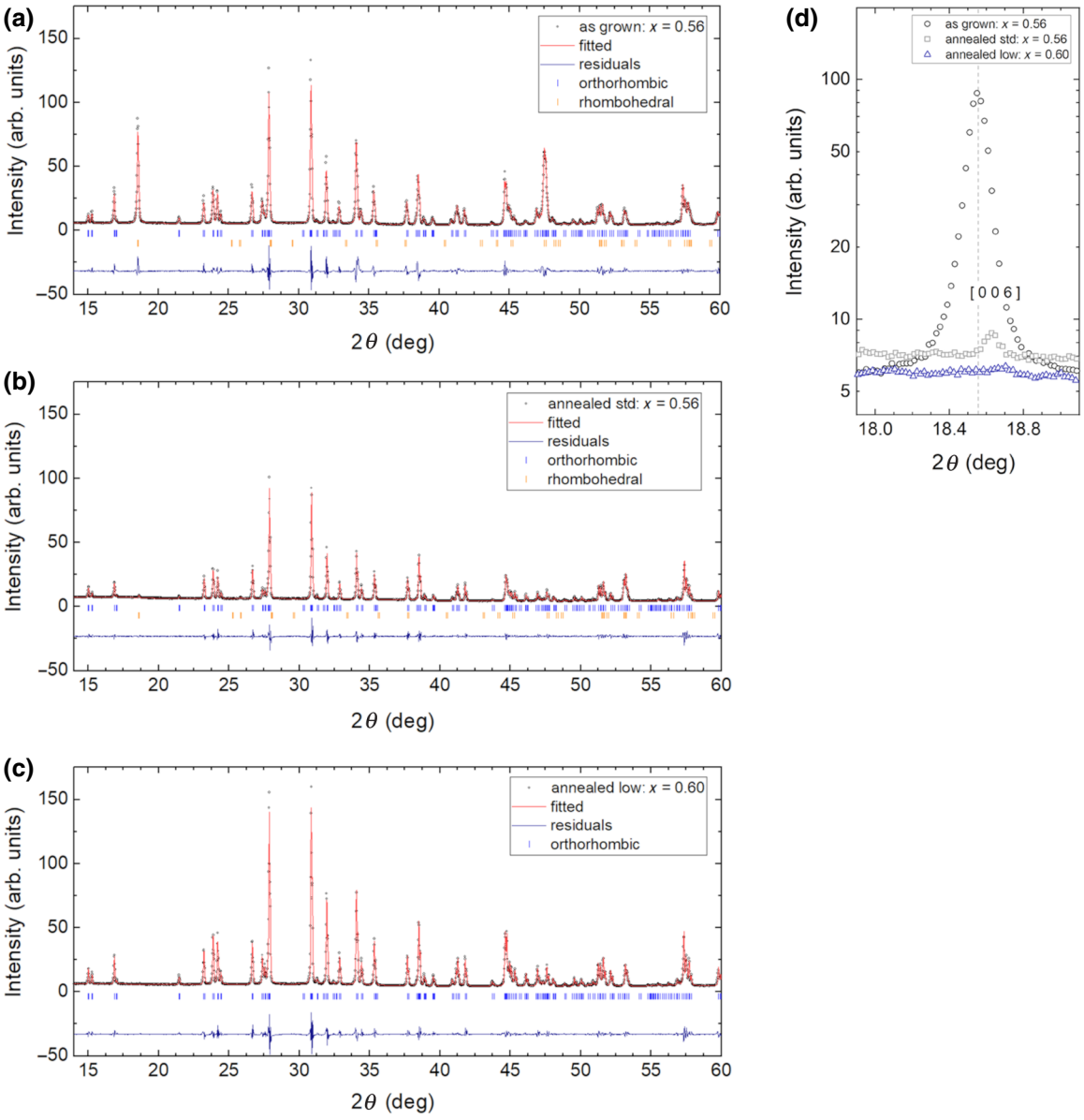

FIG. 3. XRD diffractograms for a $(Sb_{1-x}Bi_x)_2Se_3$ layer grown on SLG as grown (a), after the standard annealing process (350 °C) (b), and after a different annealing process at a nominal temperature of 360 °C (c). XRD diffractograms of the films shown in (a) and (b) need to be fitted including the rhombohedral phase, due to the (0 0 6) reflection between 18.4° and 18.8° (d). Film annealed at a nominally higher temperature does not show the rhombohedral (0 0 6) reflection, and thus, indicates an orthorhombic single phase. Vertical dashed lines show the position of the (0 0 6) reflection, according to ICDD PDF Card No. 00-033-0214. Fig. S1 within the Supplemental Material [30] shows the graph over the full 2θ range from 10° to 90°.

improves the crystal quality up to $x \approx 0.35$. For annealed SLG/Mo samples, the trend with respect to Bi substitution is not conclusive, due to the limited number of data points.

Raman measurements for the samples on SLG are shown in Fig. 4(a). For low Bi contents ($x \leq 0.06$), two main peaks are observed at 191 and 211 cm^{-1}, which can be assigned to the orthorhombic Sb_2Se_3 phase [36]. Upon incorporation of a higher Bi content, another peak arises at 177 cm^{-1} for $x = 0.177$, which shifts to lower wave numbers. The shift towards lower wave numbers with increasing Bi concentration can then be explained by the larger mass of Bi, relative to that of Sb, and a large contribution of Sb/Bi motion to this particular vibration mode. The spectra are fitted with Lorentzian functions to determine the individual peak positions and intensities for the overlapping contributions in the range between 140 and 270 cm^{-1}. Details of the fitting are shown in Fig. S4(a) within the Supplemental Material [30]. The evolution of the peak positions with respect to x is plotted in Fig. 4(b). It is demonstrated that, with increasing Bi content the peak

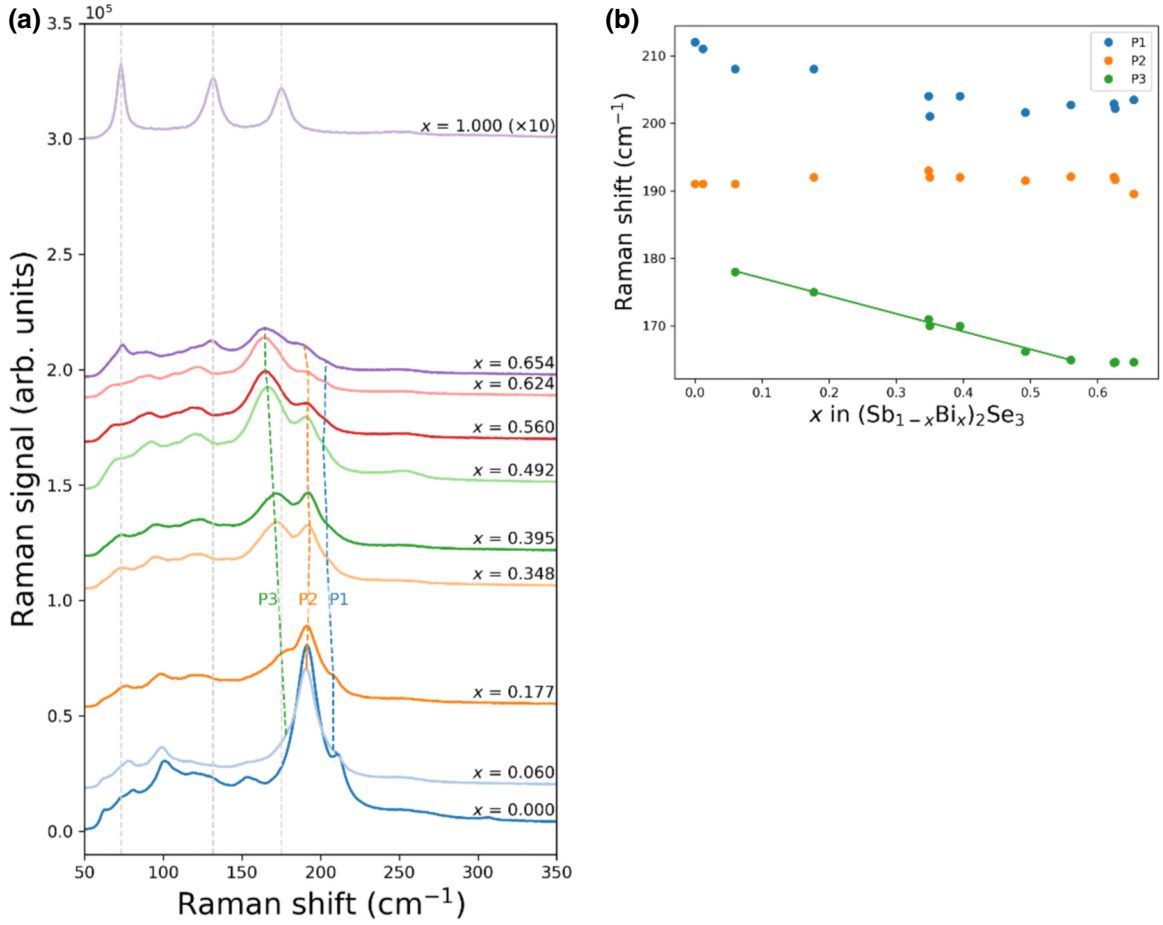

FIG. 4. (a) Raman spectra measured at room temperature for samples annealed with the standard process on SLG substrates. Spectrum for the sample with $x = 1.0$ belongs to a sample in the as-grown state (not annealed) and serves to indicate the peak positions for the rhombohedral Bi_2Se_3 phase. Shifts of the three peak positions are indicated as dashed lines in (a) and are separately plotted in (b). Solid line represents a linear fit to the peak positions of P3.

at 177 cm^{-1} (P3), shifts towards lower wave numbers and varies linearly with composition for $x > 0.06$. The fits for lower concentrations ($x < 0.06$) are found to be difficult because of the very low intensity of P3 and difficulties in disentangling it from the background. A linear fit of the position of P3 gives

$$E_{P3}(x)/\mathrm{cm}^{-1} = 179.8 - 26.3\,x. \qquad (7)$$

Additionally, we notice that the ratio of the peak intensities also behave linearly with compositions, as shown in Fig. S4(b) within the Supplemental Material [30]. The value extrapolated from Eq. (7) for pure Sb_2Se_3 (179.8 cm^{-1}) does not quite match the value for the mode that is identified at 185 cm^{-1} in single-crystal studies [37, 38], but density-functional theory calculations [37] show that other modes are present in this frequency range, which can also, in principle, account for this difference. Our data do not allow us to conclude on a precise assignment for this mode.

The Raman spectroscopy results also reveal the decomposition of the orthorhombic phase into a mixture of rhombohedral and orthorhombic. In Fig. 4(a), a sample corresponding to a pure rhombohedral Bi_2Se_3 film is included to indicate the peak positions of the rhombohedral phase. The Raman spectrum with $x = 0.654$ shows clearly the appearance of peaks belonging to the rhombohedral crystal structure of Bi_2Se_3, whereas the sample with $x = 0.624$ does not show these peaks. Thus, based on the Raman measurements, the decomposition of the $(Sb,Bi)_2Se_3$ film into the orthorhombic and rhombohedral phases is expected at a composition between $x = 0.624$ and 0.654. These values are close to, but slightly higher than, those obtained from XRD measurements. This can tentatively be explained by different volumes probed by the two techniques. Raman spectroscopy is usually more sensitive to small amounts of a given phase, but also more surface sensitive because of the low penetration depth of the laser. In contrast, XRD probes the full depth of the film. Thus, we can assume that decomposition starts from

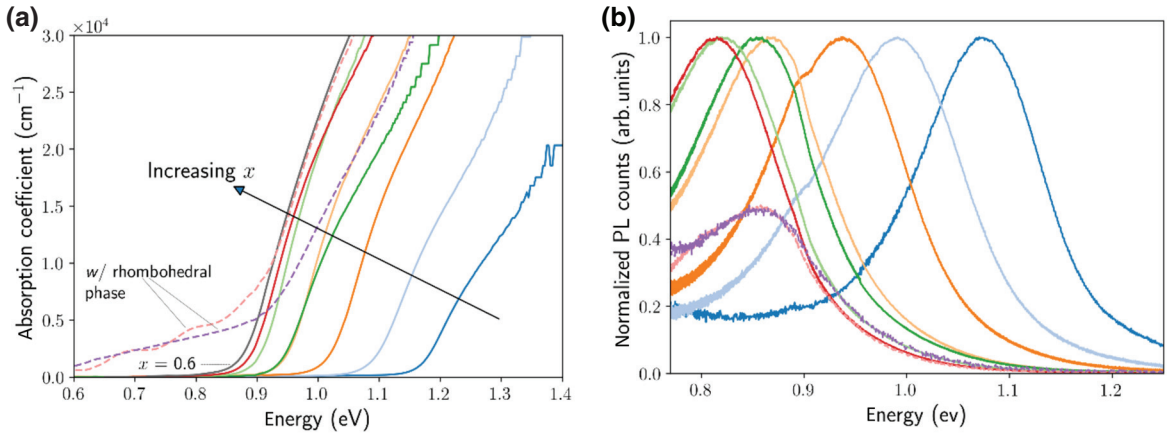

FIG. 5. (a) Absorption coefficient calculated according to Eq. (1) for the samples on SLG with the annealed std process. For higher Bi contents, the absorption edge redshifts, indicating a smaller band gap. (b) Normalized photoluminescence spectra for the same samples presented in (a), showing the redshift of the band gap as well. Samples are identical to those used for Raman measurements (see Fig. 4 for details on compositional values).

the backside of the film and is observed only in Raman measurements at higher x values compared with XRD.

Evaluation of the band gap with respect to composition is carried out on films annealed under the standard process on SLG. As-grown films are smooth, resulting in interference fringes that render a proper band-gap evaluation difficult, while films with a Mo substrate are not transparent. The annealed std samples have grain sizes in the micrometer range and are correspondingly rougher, and therefore, show no interference fringes. Figure 5(a) shows

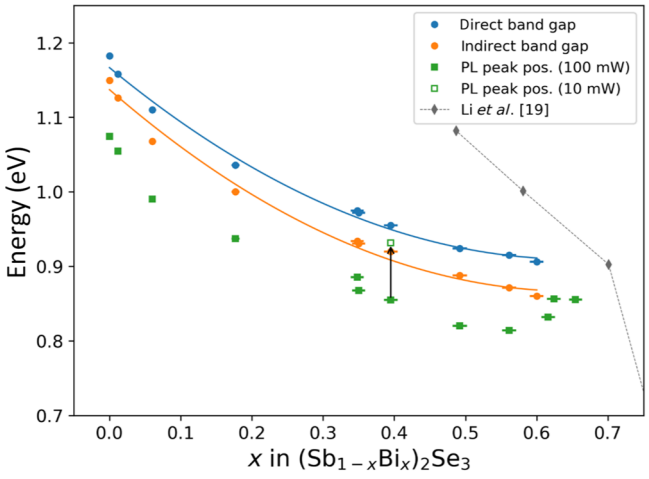

FIG. 6. Band-gap variation upon Bi incorporation. Direct and indirect band gaps are estimated from spectrophotometry. Solid lines represent an orthogonal distance fit. Peak positions from PL measurements are redshifted by 70–100 meV with respect to the indirect and direct band gaps due to heating of the laser. Open green square represents the position of the PL peak maximum measured at room temperature and a laser power of 10 mW. Band-gap data from the literature are taken from Ref. [19].

absorption data calculated for the same set of samples used for the Raman measurements (Fig. 4). Equation (1) is used for samples with a rather flat transmission below the band gap (i.e., the scaled transmission T' is used), which holds for samples dominated by the orthorhombic phase ($x \leq 0.6$, solid lines). Upon Bi incorporation into the film, a clear redshift of the absorption edge towards smaller energies is observed. The analysis using the scaled transmission T' cannot be carried out for samples showing clearly an additional rhombohedral phase in XRD (i.e., $x > 0.6$), as the transmission is not flat, but is continuously increasing up to wavelengths of 2400 nm. The absorption data for these samples are depicted in Fig. 5(a) as dashed lines, using the measured transmission T (instead of T') in Eq. (1). Consequently, the absorption coefficient is denoted with α (instead of α').

The Tauc plots used to determine the direct [Eq. (2)] and indirect [Eq. (3)] band gaps are shown in Fig. S5 within the Supplemental Material [30]. Extracted band gaps (direct and indirect) are presented in Fig. 6 as solid circles, showing a decreasing band gap with increasing x. The highest and lowest band gaps for the orthorhombic crystal structure are obtained for Sb_2Se_3 and $(Sb_{0.4}Bi_{0.6})_2Se_3$ (sample with annealed low process) with direct (indirect) band gaps of 1.182 eV (1.149 eV) and 0.906 eV (0.860 eV), respectively.

The decrease of the band gap with increasing x is estimated with an orthogonal distance fit (solid lines in Fig. 6) and results in

$$E_{g,\mathrm{direct}}/\mathrm{eV} = 1.17 - 0.79x + 0.60x^2, \quad (8)$$

$$E_{g,\mathrm{indirect}}/\mathrm{eV} = 1.14 - 0.83x + 0.64x^2. \quad (9)$$

Values for composition x and band gap can be found in Table S1 within the Supplemental Material [30]. It is noted

that straight-line behavior for the Tauc plots is more evident for the indirect transition compared with the direct one, which results in less accurate values for the direct band gap. The reason for this might be overlap of the direct and indirect transitions in the fitting range for the direct band gap. For Sb_2Se_3, the indirect transition is generally found below the direct one [39,40], in line with theoretical calculations [41,42], which report the indirect band gap between 25 and 100 meV below the direct band gap.

As expected from the band-gap values, a redshift is also observed in PL spectra depicted in Fig. 5(b), where the peak position shifts towards lower energies upon Bi incorporation. A few spectra show an asymmetric PL spectrum or a shoulder around 0.9 eV. This shoulder is caused by water vapor absorption, which cannot be completely removed by spectral correction with the calibration measurement. The PL peak positions are plotted in Fig. 6. as solid green squares and show the same trend as that of the band gaps extracted from the spectrophotometry measurements. The offset to lower energies of the PL peak position with respect to the direct and indirect band gaps of approximately 100 and 70 meV, respectively, can be associated with heating of the substrate caused by the laser during the PL measurement with a rather high laser power. The sample with the highest PL yield is also measured using only 10 mW laser power (decrease by a factor of 10), which results in a blueshift of the PL peak. The peak position at this laser power is plotted in Fig. 6 as an open green square (around $x \approx 0.4$) and agrees well with the indirect band gap determined from spectrophotometry, confirming the claim that the redshift with respect to the band gap is due to heating when measuring at 100 mW. It is noted that the PL peak position shifts continuously with the laser power between 10 and 100 mW, without changing the shape of the PL peak.

The band gap values show a discrepancy when compared with the values reported in Ref. [19] (plotted as gray diamonds in Fig. 6). A reason for this discrepancy might be the composition of the thin films given in Ref. [19], which is based on the composition of electrolytes used for electrodepositing films and not on a direct measurement of the final films.

IV. PHOTOVOLTAIC DEVICE

Figure 7(a) shows the current density-voltage characteristics of a photovoltaic device. The curve measured under dark conditions shows a reasonable single-diode-like behavior for voltages up to about 0.4 V. However, for higher forward bias voltages, a rollover is observed, i.e., the current increase with respect to voltage is smaller than that expected from an ohmic series resistance (which would yield a straight line). Such a rollover can be explained by a secondary diode in the opposite direction to the main p-n junction, for instance, located at the back contact [43]. A back barrier is observed for Sb_3Se_3-based devices grown on Mo substrates, which can no longer be observed upon the partial selenization of the Mo back contact [27]. However, $(Sb_{1-x}Bi_x)_2Se_3$ absorbers have a smaller band gap, and thus, a barrier might even be imposed by the selenized back contact (see Sec. II). The voltage, V, dependence of the dark current density $J(V)$ is fitted to a one-diode model, which is expressed as [44]

$$J(V) = J_0\left[\exp\left(\frac{V - Jr_S}{AkT}\right) - 1\right] + \frac{V - Jr_S}{R_{sh}}, \qquad (10)$$

where J_0 is the reverse saturation current density, r_S is the series resistance, A is the diode-quality factor, k is the Boltzmann constant, T is the temperature, and R_{sh} is the shunt resistance. The fit is carried out in the voltage range between -0.3 and 0.5 V and is shown in Fig.

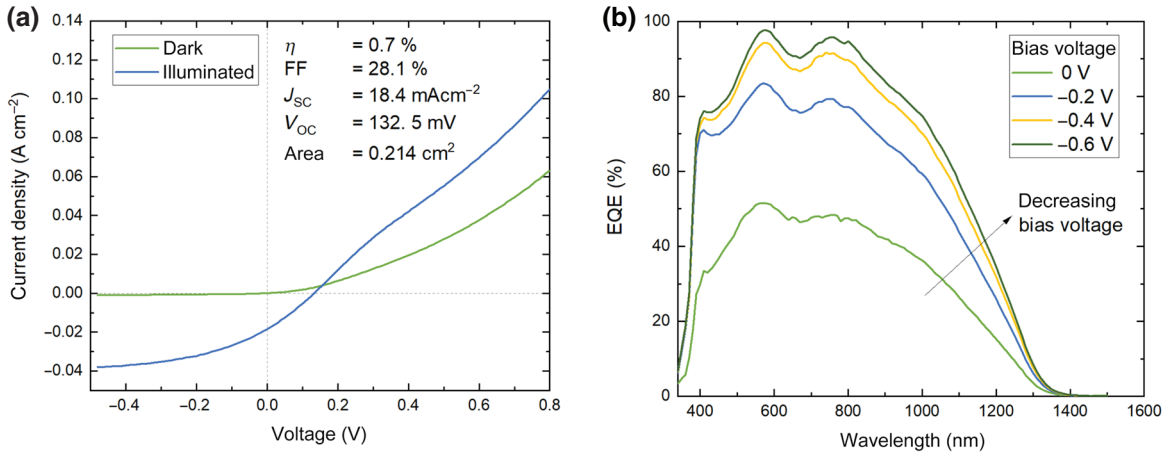

FIG. 7. (a) Current density-voltage characteristics in the dark and under one-sun illumination for a photovoltaic device with a $(Sb_{1-x}Bi_x)_2Se_3$ absorber with $x = 0.431$. (b) External quantum efficiency measured for several bias voltages. Linear extrapolation of long-wavelength response yields a band gap of 0.933 eV, as expected for the composition $x = 0.431$.

S6 within the Supplemental Material [30]. The following diode parameters are obtained: $J_O = 4.7 \times 10^{-4}$ A/cm^2, $A = 1.92$, $r_S = 11\,\Omega\,\text{cm}^2$, and $R_{\text{sh}} = 825\,\Omega\,\text{cm}^2$. Clearly, the diode exhibits a large series resistance, which might be due to a nonoptimal back contact or to poor transport within the bulk of the $(Sb,Bi)_2Se_3$ absorber. The illuminated curve shows a short-circuit current of 18.4 mA/cm^2 and a fill factor (FF) of 28.1%, resulting in a power conversion efficiency of 0.7%. A kink in the J-V curve is observed and might be caused by a barrier present in the device structure, resulting in a low fill factor. The low open-circuit voltage of 132.5 mV and the low reverse saturation current density (in the dark) of 4.7×10^{-4} A/cm^2 indicate a short carrier lifetime, which needs to be improved to use the material as a solar-cell device.

However, to use the material as an infrared detector in a photovoltaic mode, the external quantum efficiency is of primary interest and is shown in Fig. 7(b). Under short-circuit conditions, the EQE has a maximum of approximately 0.5, which might be caused by the barrier blocking extraction of the photocurrent. For reversed bias voltages, the EQE approaches unity around 600–800 nm, while losses for higher wavelengths might be caused by insufficient collection.

The band gap is extracted by linear extrapolation of the long-wavelength EQE responses and by the derivative of the EQE [45]. Independent of the bias voltage, the intercept with the ordinate yields a band gap of 0.933 eV, while the derivative gives 0.984 eV. These values are consistent with those obtained from Eq. (8) and a measured composition for this sample of $x = 0.431$ yields a direct band gap of 0.939 eV.

V. CONCLUSION

Polycrystalline thin-film $(Sb_{1-x}Bi_x)_2Se_3$ layers and photovoltaic devices are successfully fabricated using a sequential process, consisting of coevaporation of a precursor layer followed by *ex situ* annealing. Single-phase orthorhombic layers are obtained up to $x \leq 0.6$, as determined by XRD and Raman spectroscopy. For higher Bi contents $(x > 0.6)$,, the rhombohedral Bi_2Se_3 phase forms in addition. Structurally, mainly the lattice parameter, b, increases upon Bi incorporation, which is along the 1D $(Sb,Bi)_4Se_6$ ribbons. UV-vis-NIR measurements show a decrease of the direct band gap from 1.182 eV for Sb_2Se_3 to 0.906 eV for $(Sb_{0.4}Bi_{0.6})_2Se_3$, whereas the indirect band gap is roughly 30 meV lower, independently of the Bi content. This shift of the band gap(s) is also observed in PL measurements, which show band-to-band transitions at room temperature. These measurements show that the band gap can be decreased by alloying Sb_2Se_3 with Bi, and thus, opens up the possibility for its use as a short-wavelength infrared detector or a bottom cell in a multijunction photovoltaic device.

Photovoltaic devices are prepared using a CdS/ZnO n-type window layer as the front contact. Under simulated AM1.5G illumination, the nonoptimized device produces a short-circuit current density of 18.4 mA/cm^2 and an open-circuit voltage of 132.5 mV, which makes this material a candidate for the bottom cell in thin-film multijunction solar cells. The quantum efficiency under small reverse bias is above 40% at 1200 nm, where the QE of Si is already zero, demonstrating the potential of this material to be applied as an IR detector.

ACKNOWLEDGMENTS

The Luxembourg National Research Fund (FNR) and the collaboration with IEE S.A. Luxembourg is acknowledged for funding within the project ILEP. P.A. acknowledges the University of Luxembourg IRP LASER2 project for funding. D.S. acknowledges funding by the FNR through the MASSENA project (Grant No. PRIDE/15/10935404).

[1] M. A. Green, Y. Hishikawa, E. D. Dunlop, D. H. Levi, J. Hohl-Ebinger, M. Yoshita, and A. W. Y. Ho-Baillie, Solar cell efficiency tables (version 53), Prog. Photovolt.: Res. Appl. **27**, 3 (2019).

[2] W. Shockley and H. J. Queisser, Detailed balance limit of efficiency of p-n junction solar cells, J. Appl. Phys. **32**, 510 (1961).

[3] T. Kirchartz and U. Rau, What makes a good solar cell?, Adv. Energy Mater. **8**, 1703385 (2018).

[4] C. A, Teixeira Dos Santos, M. Lopo, R. N. M. J. Páscoa, and J. A. Lopes, A review on the applications of portable near-infrared spectrometers in the agro-food industry, Appl. Spectrosc. **67**, 1215 (2013).

[5] N. Prieto, O. Pawluczyk, M. E. R. Dugan, and J. L. Aalhus, A review of the principles and applications of near-infrared spectroscopy to characterize meat, Fat, and meat products, Appl. Spectrosc. **71**, 1403 (2017).

[6] P. Werle, F. Slemr, K. Maurer, R. Kormann, R. Mücke, and B. Jänker, Near- and mid-infrared laser-optical sensors for gas analysis, Opt. Lasers Eng. **37**, 101 (2002).

[7] A. Samman, L. Rimai, J. R. McBride, R. O. Carter, W. H. Weber, C. Gmachl, F. Capasso, A. L. Hutchinson, D. L. Sivco, and A. Y. Cho, in *IEEE Vehicular Technology Conference* (2000).

[8] A. Rogalski, History of infrared detectors, Opto-Electron. Rev. **20**, 279 (2012).

[9] A. Rogalski, Hgcdte infrared detector material: History, status and outlook, Rep. Prog. Phys. **68**, 2267 (2005).

[10] A. Rogalski, J. Antoszewski, and L. Faraone, Third-generation infrared photodetector arrays, J. Appl. Phys. **105**, 091101 (2009).

[11] R. Saran and R. J. Curry, Lead sulphide nanocrystal photodetector technologies, Nat. Photonics **10**, 81 (2016).

[12] C. R. Kagan, E. Lifshitz, E. H. Sargent, and D. V. Talapin, Building devices from colloidal quantum dots, Science **353**, aac5523 (2016).

[13] J. P. Clifford, G. Konstantatos, K. W. Johnston, S. Hoogland, L. Levina, and E. H. Sargent, Fast, sensitive and spectrally tuneable colloidal-quantum-dot photodetectors, Nat. Nanotechnol. **4**, 40 (2009).

[14] E. J. D. Klem, C. Gregory, D. Temple, and J. Lewis, in *Proceedings of SPIE - The International Society for Optical Engineering* (2015).

[15] G. Konstantatos and E. H. Sargent, Nanostructured materials for photon detection, Nat. Nanotechnol. **5**, 391 (2010).

[16] M. Birkett, W. M. Linhart, J. Stoner, L. J. Phillips, K. Durose, J. Alaria, J. D. Major, R. Kudrawiec, and T. D. Veal, Band gap temperature-dependence of close-space sublimation grown Sb_2Se_3 by photo-reflectance, APL Mater. **6**, 084901 (2018).

[17] H. Lei, J. Chen, Z. Tan, and G. Fang, Review of recent progress in antimony chalcogenide-based solar cells: Materials and devices, Solar RRL **3**, 1900026 (2019).

[18] Z. Li, X. Liang, G. Li, H. Liu, H. Zhang, J. Guo, J. Chen, K. Shen, X. San, W. Yu, R. E. I. Schropp, and Y. Mai, 9.2%-efficient core-shell structured antimony selenide nanorod array solar cells, Nat. Commun. **10**, 125 (2019).

[19] J. Li, B. Wang, F. Liu, J. Liu, M. Jia, Y. Lai, and Y. Liu, Structural and optical properties of electrodeposited $Bi_{2-x}Sb_xSe_3$ thin films, ECS Solid State Lett. **1**, Q29 (2012).

[20] S. Wang, Y. Sun, J. Yang, B. Duan, L. Wu, and W. Zhang, High thermoelectric performance in Te-free $(Bi, Sb)_2Se_3$: Via structural transition induced band convergence and chemical bond softening, Energy Environ. Sci. **9**, 3436 (2016).

[21] Y. Liu, C. Chong, W. Chen, J. A. Huang, C. Cheng, K. Tsuei, Z. Li, H. Qiu, and V. V. Marchenkov, Growth and characterization of MBE-grown $(Bi_{1-x}Sb_x)_2Se_3$ topological insulator, Jpn. J. Appl. Phys. **56**, 070311 (2017).

[22] J. Liu and D. Vanderbilt, Topological phase transitions in $(Bi_{1-x}In_x)_2Se_3$ and $(Bi_{1-x}Sb_x)_2Se_3$, Phys. Rev. B: Condens. Matter Mater. Physi. **88**, 224202 (2013).

[23] C. Chen, D. C. Bobela, Y. Yang, S. Lu, K. Zeng, C. Ge, B. Yang, L. Gao, Y. Zhao, M. C. Beard, and J. Tang, Characterization of basic physical properties of Sb_2Se_3 and its relevance for photovoltaics, Front. Optoelectron. **10**, 18 (2017).

[24] X. Liu, X. Xiao, Y. Yang, D. J. Xue, D. B. Li, C. Chen, S. Lu, L. Gao, Y. He, M. C. Beard, G. Wang, S. Chen, and J. Tang, Enhanced Sb_2Se_3 solar cell performance through theory-guided defect control, Prog. Photovolt.: Res. Appl. **25**, 861 (2017).

[25] K. J. Tiwari, M. Neuschitzer, M. Espíndola, Y. Sanchez, P. Vidal, E. Saucedo, and P. Malar, in *2018 IEEE 7th World Conference on Photovoltaic Energy Conversion, WCPEC 2018 - A Joint Conference of 45th IEEE PVSC, 28th PVSEC and 34th EU PVSEC* (2018).

[26] C. N. Savory and D. O. Scanlon, The complex defect chemistry of antimony selenide, J. Mater. Chem. A **7**, 10739 (2019).

[27] Z. Li, X. Chen, H. Zhu, J. Chen, Y. Guo, C. Zhang, W. Zhang, X. Niu, and Y. Mai, Sb_2Se_3 thin film solar cells in substrate configuration and the back contact selenization, Sol. Energy Mater. Sol. Cells **161**, 190 (2017).

[28] C. Hönes, Dissertation - Docteur en Physique, University of Luxembourg, 2016.

[29] W. E. Vargas, D. E. Azofeifa, and N. Clark, Retrieved optical properties of thin films on absorbing substrates from transmittance measurements by application of a spectral projected gradient method, Thin Solid Films **425**, 1 (2003).

[30] See the Supplemental Material at http://link.aps.org/supplemental/10.1103/PhysRevApplied.14.024014 for additional figures and information.

[31] P. Yu and M. Cardona, *Fundamentals of Semicondcutors*, 4 Ed. (Springer-Verlag, Berlin Heidelberg, 2010).

[32] J. Rodríguez-Carvajal, Recent advances in magnetic structure determination by neutron powder diffraction, Phys. B: Phys. Condens. Matter **192**, 55 (1993).

[33] J. Rodríguez-Carvajal and T. Roisnel, Line broadening analysis using fullprof: Determination of microstructural properties, Mater. Sci. Forum **443-444**, 123 (2004).

[34] K. Momma and F. Izumi, VESTA 3 for three-dimensional visualization of crystal, volumetric and morphology data, J. Appl. Crystallogr. **44**, 1272 (2011).

[35] X. Liu, J. Chen, M. Luo, M. Leng, Z. Xia, Y. Zhou, S. Qin, D. J. Xue, L. Lv, H. Huang, D. Niu, and J. Tang, Thermal evaporation and characterization of Sb_2Se_3 thin film for substrate Sb_2Se_3/CdS solar cells, ACS Appl. Mater. Interfaces **6**, 10687 (2014).

[36] A. Shongalova, M. R. Correia, B. Vermang, J. M. V. Cunha, P. M. P. Salomé, and P. A. Fernandes, On the identification of Sb_2Se_3 using Raman scattering, MRS Commun. **8**, 865 (2018).

[37] N. Fleck, T. D. C. Hobson, C. N. Savory, J. Buckeridge, T. D. Veal, M. R. Correia, D. O. Scanlon, K. Durose, and F. Jäckel, Identifying Raman modes of Sb_2Se_3 and their symmetries using angle-resolved polarised Raman spectra, J. Mater. Chem. A **8**, 8337 (2020).

[38] P. Vidal-Fuentes, M. Guc, X. Alcobe, T. Jawhari, M. Placidi, A. Pérez-Rodríguez, E. Saucedo, and V. I. Roca, Multiwavelength excitation Raman scattering study of Sb_2Se_3 compound: Fundamental vibrational properties and secondary phases detection, 2D Mater. **6**, 045054 (2019).

[39] C. Chen, W. Li, Y. Zhou, M. Luo, X. Liu, K. Zeng, B. Yang, C. Zhang, J. Han, and J. Tang, Optical properties of amorphous and polycrystalline Sb_2Se_3 thin films prepared by thermal evaporation, Appl. Phys. Lett. **107**, 043905 (2015).

[40] H. El-Shair, A. Ibrahim, E. Abd El-Wahabb, M. Afify, and F. Abd El-Salam, Optical properties of Sb_2Se_3 thin films, Vacuum **42**, 911 (1991).

[41] L. J. Phillips, C. N. Savory, O. S. Hutter, P. J. Yates, H. Shiel, S. Mariotti, L. Bowen, M. Birkett, K. Durose, D. O. Scanlon, and J. D. Major, Current enhancement via a TiO_2 window layer for CSS Sb_2Se_3 solar cells: Performance limits and high V_{oc}, IEEE J. Photovolt. **9**, 544 (2019).

[42] M. R. Filip, C. E. Patrick, and F. Giustino, GW quasiparticle band structures of stibnite, antimonselite, bismuthinite, and guanajuatite, Phys. Rev. B: Condens. Matter Mater. Phys. **87**, 205125 (2013).

[43] A. Niemegeers and M. Burgelman, Effect of the Au/CdTe back contact on IV and CV characteristics of

Au/CdTe/CdS/TCO solar cells, J. Appl. Phys. **81**, 2881 (1997).

[44] A. R. Burgers, J. A. Eikelboom, A. Schonecker, and W. C. Sinke, in *Conference Record of the IEEE Photovoltaic Specialists Conference* (1996).

[45] R. Carron, C. Andres, E. Avancini, T. Feurer, S. Nishiwaki, S. Pisoni, F. Fu, M. Lingg, Y. E. Romanyuk, S. Buecheler, and A. N. Tiwari, Bandgap of thin film solar cell absorbers: A comparison of various determination methods, Thin Solid Films **669**, 482 (2019).